Therapeutic Targeting and Structural Characterization of a Sotorasib-Modified KRAS G12C–MHC I Complex Demonstrate the Antitumor Efficacy of Hapten-Based Strategies

Apurva Pandey[1], Peter J. Rohweder[2], Lieza M. Chan[3], Chayanid Ongpipattanakul[2], Dong hee Chung[2], Bryce Paolella[2], Fiona M. Quimby[1], Ngoc Nguyen[1], Kliment A. Verba[3], Michael J. Evans[1], and Charles S. Craik[2]

ABSTRACT

Antibody-based therapies have emerged as a powerful strategy for the management of diverse cancers. Unfortunately, tumor-specific antigens remain challenging to identify and target. Recent work established that inhibitor-modified peptide adducts derived from KRAS G12C are competent for antigen presentation via MHC I and can be targeted by antibody-based therapeutics, offering a means to directly target an intracellular oncoprotein at the cell surface with combination therapies. Here, we validated the antigen display of "haptenated" KRAS G12C peptide fragments on tumors in mouse models treated with the FDA-approved KRAS G12C covalent inhibitor sotorasib using PET/CT imaging of an ^{89}Zr-labeled P1B7 IgG antibody, which selectively binds sotorasib-modified KRAS G12C–MHC I complexes. Targeting this peptide–MHC I complex with radioligand therapy using ^{225}Ac- or ^{177}Lu-P1B7 IgG effectively inhibited tumor growth in combination with sotorasib. Elucidation of the 3.1 Å cryo-EM structure of P1B7 bound to a haptenated KRAS G12C peptide–MHC I complex confirmed that the sotorasib-modified KRAS G12C peptide is presented via a canonical binding pose and showed that P1B7 binds the complex in a T-cell receptor–like manner. Together, these findings demonstrate the potential value of targeting unique oncoprotein-derived, haptenated MHC I complexes with radioligand therapeutics and provide a structural framework for developing next generation antibodies.

Significance: Radioligand therapy using an antibody targeting KRAS-derived, sotorasib-modified MHC I complexes elicits antitumor effects superior to those of sotorasib alone and provides a potential strategy to repurpose sotorasib as a hapten to overcome resistance.

Introduction

Targeting tumor-associated antigens is a central tenet of antibody-based therapies, but truly tumor-*specific* antigens are exceedingly rare. One of the most attractive and intuitive classes of targets is oncoproteins, as they are intrinsically tumor-specific. However, oncoproteins are typically intracellular, precluding the development of antibody-based therapeutics that directly target them at the cell surface. Additionally, oncoproteins differ from their cognate wild-type (WT) proteins by very few mutations, most commonly a single point mutation, making their specific targeting even more challenging as distinguishing them from the WT protein must be achieved based on minor chemical differences. One such potential oncoprotein target is KRAS, which is mutated in approximately 20% of all cancers (1, 2). Recently, covalent inhibitors of the KRAS G12C mutant have been developed and shown efficacy in the clinical management of G12C mutant cancers (3, 4). By forming an irreversible bond with the acquired cysteine, these drugs inhibit the mutated KRAS protein but are unable to react with the WT protein. Because of the irreversible nature of these inhibitors, the drug-modified cysteine is maintained through the lifecycle of the protein. Previously, we and others established that KRAS G12C proteins covalently modified with irreversible inhibitors can be processed and presented as peptide fragments bearing this covalent modification in MHC I complexes at the cell surface (5, 6). The antigen presentation process offers a unique opportunity for therapeutic targeting as it relocates an intracellular antigen to the cell surface where it is accessible to antibody therapeutics (7–11). The presentation of inhibitor-modified KRAS G12C peptides results in a highly unique neoantigen, converting the mutant cysteine residue into a relatively large and unique chemical epitope, which is amenable to antibody recognition. This approach repurposes the covalent inhibitor as a "hapten," or a small molecule that is not immunogenic on its own but can elicit an immune response when bound to a carrier protein (12, 13). Repurposing the preclinical KRAS G12C inhibitor ARS1620 as a hapten, we demonstrated that targeting of these haptenated MHC I complexes with bispecific T-cell engagers resulted in robust anticancer responses. In order to translate this approach further, we also identified antibodies that bind to the FDA-approved KRAS G12C inhibitor sotorasib, including P1B7, an antibody with high

[1]Department of Radiology and Biomedical Imaging, University of California, San Francisco, San Francisco, California. [2]Department of Pharmaceutical Chemistry, University of California, San Francisco, San Francisco, California. [3]Department of Cellular and Molecular Pharmacology, University of California, San Francisco, San Francisco, California.

A. Pandey, P.J. Rohweder, and L.M. Chan contributed equally to this article.

Corresponding Authors: Kliment A. Verba, Department of Cellular and Molecular Pharmacology, University of California, San Francisco, 600 16th Street, Room S412E, San Francisco, CA 94143. E-mail: kliment.verba@ucsf.edu; Michael J. Evans, Department of Radiology and Biomedical Imaging, University of California, San Francisco, 600 16th Street, Room N572C, San Francisco, CA 94143. E-mail: michael.evans@ucsf.edu; and Charles S. Craik, Department of Pharmaceutical Chemistry, University of California, San Francisco, 600 16th Street, Room S-512C, Box 2280, San Francisco, CA 94143. E-mail: Charles.Craik@ucsf.edu

Cancer Res 2025;85:329–41

doi: 10.1158/0008-5472.CAN-24-2450

affinity and specificity for these sotorasib-modified MHC I complexes (5). In parallel, others demonstrated that targeting of these sotorasib-derived MHC I complexes was effective, corroborating the initial study with the preclinical ARS1620 (6). In both studies, these hapten-targeted therapies maintained efficacy even in the case of resistance to inhibitor monotherapy. These results indicate that combination therapies with inhibitors and hapten-targeted antibodies can offer superior efficacy to inhibitor monotherapy as well as a means to reclaim therapeutic efficacy in the case of resistance to the covalent inhibitor monotherapy.

Although previous work had focused on the development of T cell–engaging therapies, clinical development of T cell–based therapeutics remains challenging for solid tumors due to tumor heterogeneity, poor tumor penetration of immune effectors, and the immunosuppressive tumor microenvironment (14, 15). Additionally, MHC I complexes of a target peptide are presented in low abundance and can be heterogeneously expressed, making their targeting even more difficult (16, 17). In exploring alternative therapeutic approaches, we hypothesized that arming antibodies with therapeutic radioisotopes could overcome the anticipated challenges with T cell–based therapeutics. For example α- and β-particles are exquisitely potent and do not require high receptor copy number (i.e., ~10^5 per cell) to confer sufficient genotoxicity for antitumor effects (18). Moreover, α- and β-particles can deposit ionizations over distances that exceed one cell diameter, and we hypothesized that crossfire effects could overcome the heterogeneous expression of peptide–MHC I complexes within tumors. On this basis, we radiolabeled P1B7 with actinium-225 (^{225}Ac) or lutetium-177 (^{177}Lu), clinically active radioisotopes that produce α- and β-particles, respectively, and tested their antitumor efficacy *in vivo*. In order to enable the development of next generation antibodies, we have also solved the structure of P1B7 bound to the sotorasib-haptenated A*03:01 MHC I complex using cryo-EM, providing an atomic understanding of this unique antigen.

Materials and Methods

Lead contact

Further information and requests for resources and reagents (**Table 1**) should be directed to and will be fulfilled by the lead contact, C.S. Craik.

Table 1. Key resources.

Resource	Source	RRID/identification
Antibodies		
P1B7 IgG	Generated in this study	N/A
Bacterial strains		
5-alpha *E. coli*	NEB	Cat. No. C2987H
BL21(DE3) *E. coli*	NEB	Cat. No. C2527H
Biological samples		
Nu/J mice, male	Jackson Laboratory	RRID: RIMSR_JAX:002019
Chemical reagents		
KRas peptides (K5, V7)	Synthesized in house	N/A
Fos1 peptide	Synthesized in house	N/A
Sotorasib	MedChemExpress	Cat. No. HY-114277
Adagrasib	MedChemExpress	Cat. No. HY-130149
Macropa-$(PEG)_4$-TFP	Flavell Lab UCSF	N/A
p-SCN-Bn-Deferoxamine	Macrocyclics	Cat. No.B-705
p-SCN-Bn-DOTA	Macrocyclics	Cat. No.B-205
$^{89}Zr(oxalate)_4$	3D Imaging, LLC	N/A
$^{177}LuCl_3$	Oak Ridge National Laboratory	N/A
$^{225}Ac(NO_3)_3$	Oak Ridge National Laboratory	N/A
NHS-Fluorescein	Thermo Fisher Scientific	Cat. No 46409
Critical commercial reagents and kits		
Gold holey carbon 1.2/1.3 400 mesh grids	Quantifoil	N/A
ExpiFectamine 293 Transfection Kit	Thermo Fisher Scientific	Cat. No.A14524
Deposited data		
P1B7•V7-Sotorasib•A*03:01 cryo-EM structure	N/A	PDB: 8UDR
Experimental models: Cell lines		
H358	ATCC	RRID: CVCL_1559
UMUC3	ATCC	RRID: CVCL_1783
Expi293F	Gibco	RRID: CVCL_D615
Recombinant DNA		
Plasmid: P1B7 heavy chain and light chain	Generated in this study, Twist Biosciences	N/A
Software and algorithms		
Amide	SourceForge	RRID: SCR_005940
GraphPad Prism 10.2.3	GraphPad	RRID: SCR_002798
SerialEM	UC Boulder	RRID: SCR_017293
CryoSPARC v3.2.0	Structura Biotechnology Inc.	RRID: SCR_016501
UCSF ChimeraX	UC San Francisco	RRID: SCR_015872

(Continued on the following page)

Table 1. Key resources. (Cont'd)

Resource	Source	RRID/identification
Isolde	Cambridge Institute for Medical Research	RRID: SCR_025577
RosettaScripts	Rosetta Commons	RRID: SCR_015701
Coot	MRC Laboratory of Molecular Biology	RRID: SCR_014222
Phenix	Lawrence Berkeley Laboratory	RRID: SCR_014224
PISA	EMBL-EMI	RRID: SCR_015749
FlowJo 10.10	BD	RRID: SCR_008520
R Software	R project	RRID: SCR_001905
MotionCor2	UC San Francisco	RRID: SCR_016499
Instruments		
AKTA pure	Cytiva	RRID: SCR_023461
Octet RED384	Sartorius	RRID: SCR_023267
CytoFLEX Analyzer	Beckman	RRID: SCR_019627
Syro II peptide synthesizer	Biotage	RRID: SCR_025775
SP GeneVac EZ-2 4.0	SP Scientific	RRID: SCR_017367
Waters Acquity UPLC	Waters	RRID: SCR_025677
Waters Xevo G2-XS	Waters	RRID: SCR_020885
ND-1000 Spectrophotometer	Thermo Fisher Scientific	RRID: SCR_016517
Micro PET/CT scanner	Inveon, Siemens Healthcare	N/A
Hidex automatic gamma counter	Hidex	RRID: SCR_025751
FEI Vitrobot Mark IV	Thermo Fisher Scientific	RRID: SCR_025773
Titan Krios G2 @ UCSF advanced microscopy core facility	Thermo Fisher Scientific	RRID: SCR_025781
K3 Camera	GATAN	RRID: SCR_019937

Materials availability

We will share all expression plasmids upon request and signing of a material transfer agreement.

Experimental model and subject details

Cell lines

UMUC3 (bladder, male, RRID: CVCL_1783) and NCI-H358 (lung, male, RRID: CVCL_1559) cells were maintained in DMEM (Gibco) + 10% FBS (Gibco) + 1 % penicillin (10,000 U/mL) and streptomycin (10,000 μg/mL, Gibco). NCI-H358 cells were received from ATCC and reported negative for *Mycoplasma* by them. UMUC3 cells were originally received from ATCC and provided by the laboratory of Professor Jonathan Chou where they were validated by short tandem repeat DNA profiling and tested negative for *Mycoplasma* (MycoAlert, Lonza) before handoff of frozen stocks. All cell line experiments were conducted within 6 months and ~20 to 30 passages from obtaining them from the ATCC or after being thawed from cryopreservation. No further authentication or *Mycoplasma* testing was performed.

Animal studies

All animal experiments were approved by the Institutional Animal Care and Use Committee at University of California, San Francisco (IACUC protocol n. AN191219-01ZI). Six- to eight-week-old male Nu/J mice (RRID: RIMSR_JAX:002019) were purchased from The Jackson Laboratory and housed with free access to the water and food. Mice were inoculated with either 4×10^6 UMUC3 or H358 cells in a mixture of media and Matrigel (Corning; v/v 1:1, 100 μL) subcutaneously into the left shoulder (imaging) or left flank (therapy). Imaging/therapy studies were initiated when the tumor size reached 100 to 150 mm^3 12 to 14 days after inoculation.

Data analysis and statistical considerations

All *in vivo* PET data were analyzed using open-source Amide software (amide.sourceforge.net, RRID: SCR_005940). Reported static (single time-point data) reflects gamma counting of harvested tissues. An unpaired, two-tailed Student *t* test was performed in Prism (v10.2.3, RRID: SCR_002798) to determine statistically significant differences between two treatment arms in PET imaging studies. To evaluate if the tumor volume changes across the time and if the tumor volumes are different across the treatment arms, we used linear mixed models with $\log_{10}$ transformation of the tumor volume, in which mouse was considered as the random effect, whereas time and arm were considered as the fixed effects. The linear mixed model was fit by using R (version 4.3.2, RRID: SCR_001905). In all cases, P values < 0.01 were reported as statistically significant.

General methods

All starting materials were purchased from Acros Organics, Alfa Aesar, Sigma Aldrich, or TCI America and used without further purification. Sotorasib and adagrasib were purchased from MedChemExpress and used without further purifications (HY-114277, HY-130149). It was formulated in 10% DMSO, 40% PEG-300, and 50% PBS for administration via oral gavage. Purity analysis of expressed IgGs was done via chromatography and SDS-PAGE. Purity analysis of all compounds employed in biological experiments was determined by radio instant thin layer chromatography (iTLC) analysis of the radioactive complex species. Percent purity as determined by radio iTLC is reported individually for each compound; representative iTLC traces employed for purity analysis are provided within the supporting information. iTLC: iTLC-SG (Gelman Science Inc.). Method A = mobile phase 20 mmol/L citric acid (pH = 2). Free $^{89}Zr/^{177}Lu/^{225}Ac$ moves with solvent front, and bound $^{89}Zr/^{177}Lu/^{225}Ac$ stays at the origin. Radiolabeling was carried out using a general protocol for all compounds reported.

Identification of antibodies from Fab-phage display libraries

The antibodies used in this study have been previously reported and full methodology for their isolation and characterization can be found in that publication (5, 19). Briefly, we used a previously described human naïve B-cell phage display library with a diversity of

4.1×10^{10} to identify Fabs against a sotorasib-labeled MHC I complex. Fabs were isolated using a previously described protocol (20). Briefly, the antigen (V7–sotorasib A*03:01 MHC I complex) was immobilized using streptavidin magnetic beads (Invitrogen) and exposed to the Fab-phage library for four rounds of panning. Negative selection was done in rounds 3 and 4 with the cognate V7 WT A*03:01 MHC I complex. After four rounds of selection, individual clones were screened in an ELISA for binding to the target antigen. Clones with a positive signal were sequenced and unique clones were expressed in BL21(DE3) *E. coli* (NEB) and purified for further analysis.

Expression of P1B7 IgG

Mammalian expression constructs for the heavy and light chains were synthesized by Twist Bioscience. DNA fragments encoding the heavy chain of the P1B7 Fab isolated from the phage display library were appended to the human IgG1 heavy chain sequence and cloned into a pTT5 expression vector with a signal peptide (MKHLWFFLLLVAAPRWVLS). The light chain sequence was taken directly from the Fab-phage constructs and cloned into a pTT5 vector with a signal peptide (MVLQTQVFISLLLWISGAYG). Expi293F cells (Gibco, RRID: CVCL_D615) were used as supplied with no further testing and maintained in Expi293 expression medium. On the day before transfection, cells were diluted to 3.0×10^6 cells/mL and then diluted again on the day of transfection back to 3.0×10^6 cells/mL. Transfection was performed with ExpiFectamine (Thermo Fisher Scientific) reagent following the manufacturer's instructions using 1 μg plasmid per mL culture (0.5 μg heavy chain–encoding plasmid and 0.5 μg light chain–encoding plasmid). After 5 days, cells were pelleted by centrifugation (4,000 × *g*, 5 minutes) and combined with an equal volume of 1× PBS before filtering the supernatant through a 0.2-μm PES membrane filter. The filtrate was purified at 4°C using a protein A affinity column (HiTrap MabSelect Xtra 1 mL) using an Äkta pure system (Cytiva, RRID: SCR_023461). Column was pre-equilibrated with five column volumes of 1× PBS pH 7.4. Filtrate was then applied to column at 4 mL/minutes, and column was washed with five column volumes of 1× PBS pH 7.4. Captured IgG was eluted with pH 3.0 glycine buffer (100 mmol/L) in three fractions of 3 mL and immediately quenched with 0.75 mL of 1 mol/L pH 8 Tris buffer. Quenched elution fractions were pooled and concentrated to a volume of 1 mL. The sample was applied at 4°C to a pre-equilibrated (1.2 column volumes 1× PBS) size exclusion chromatography (SEC) column (Superdex200 increase 10–300; CV-24 mL) by inlet injection. SEC running buffer (1× PBS pH 7.4) flowrate was 0.75 mL/minutes for 1.5 column volumes. Elution was collected in 0.5-mL fractions on a 96-well plate. Purified IgG fractions were pooled and subjected to SDS-PAGE and DSF analysis.

Binding measurements via Octet

Binding of P1B7 IgG was confirmed using an Octet RED384 instrument (Sartorius, RRID: SCR_023267) as previously described (5). MHC I complex (125 nmol/L in 1% BSA/PBS) was immobilized on Sartorius streptavidin SA biosensors for all assays. All measurements were performed in 1% BSA PBS pH 7.4 in 384 well plates. P1B7 IgG was qualitatively tested via Octet to confirm functional protein before and after chelator conjugation steps as quality control. Full dose response experiments with V7-510 A*03:01 and K5-510 A*02:01 employed IgG ranging from 4 μmol/L to 0.98 nmol/L using 2× dilutions. Association steps were carried out for 10 minutes, and dissociation steps were carried out for 5 minutes. A repeated standard 62.5 nmol/L IgG condition was done in each run and used to normalize for slight variations between antigen loading density between consecutive runs. The binding response (nm) at 120 seconds was plotted against IgG concentration and fit using a nonlinear reduction in Prism to derive EC_{50} values.

P1B7 Fab-phage binding characterization via RAPID flow cytometry

RAPID flow cytometry was performed using previously described (21). Briefly, freshly prepared phage displaying P1B7 as a Fab was chemically labeled with NHS-FITC (Thermo Fisher Scientific). Each MHC I complex (V7-510 A*03:01, K5-510 A*03:01, FosI-510 A*03:01) was immobilized to SPHERO streptavidin polystyrene bead particles (3.0–3.9 μm) at 10 nmol/L final concentration per 100 μL of beads in 1%BSA PBS. After 1 hour of incubation, samples were washed with 1% BSA PBS to remove any nonspecific binding. Flow cytometry analysis was performed on a benchtop Beckman Cytoflex Analyzer (RRID: SCR_019627). Single bead populations were gated with FSC and SSC parameters, followed by gating linear FSA and FSW. The final histogram analysis was done with FITC-A.

MHC I refolding and purification

MHC heavy chain and β-2 microglobulin (B2m) were expressed and purified following a previously reported protocol and used in Octet experiments to quality control P1B7 IgG (5, 22). MHC I heavy chain plasmids containing BirA tags at the C-terminus were transformed into BL21(DE3) *E. coli* coexpressing for *in cellulo* biotinylation. BirA refolding reactions were performed with various peptides of interest in refolding buffer [100 mmol/L Tris pH 8.0, 400 mmol/L L-Arginine•HCl, 5 mmol/L reduced glutathione, 0.5 mmol/L oxidized glutathione, 2 mmol/L EDTA, and complete protease inhibitor cocktail (Roche)]. Briefly, B2m (2 μmol/L) and peptide (10 μmol/L) were diluted into refolding buffer, and then denatured heavy chain was added to 1 μmol/L. Reactions proceeded at 10°C for 72 hours. MHC I complexes were purified by SEC as described above in Expression of P1B7 IgG using an isocratic method with a Tris buffer (20 mmol/L, pH = 7.0, 150 mmol/L NaCl). Fast protein liquid chromatography fractions were tested via SDS-PAGE. Peptides used for MHC I complexes: V7-510 [VVVGAC(Sotorasib)GVGK], K5-510 [KLVVVGAC(Sotorasib)GV], and Fos1-510 [VLEAHRPIC(Sotorasib)K].

Peptide synthesis and purification

Peptides were synthesized using a Syro II peptide synthesizer (Biotage, RRID: SCR_025775) using standard *N-(9-fluorenyl) methoxycarbonyl* (FMOC) solid phase synthesis as previously described (5). All peptides were synthesized at 12.5 μmol scale using preloaded Wang resin at ambient temperature. All coupling reactions were done with 4.9 eq of *O*-(*1H*-6-chlorobenzotriazole-1-yl)-1,1,3,3-tetramethyluronium hexafluoro-phosphate, 5 eq of FMOC-AA-OH, and 20 eq of *N*-methylmorpholine in 500 μL of *N,N*-dimethyl formamide (DMF). Each amino acid position was double-coupled with 8-minute reactions. FMOC-protected N-termini were deprotected with 500 μL 40% 4-methypiperidine in DMF for 3 minutes, followed by 500 μL 20% 4-methypiperidine in DMF for 10 minutes and six washes with 500 μL of DMF for 3 minutes. Biotinylation of the N-terminus as performed on resin using 5 eq biotin, 4.9 eq *O*-(*1H*-6-chlorobenzotriazole-1-yl)-1,1,3,3-tetramethyluronium hexafluoro-phosphate, and 20 eq *N*-methylmorpholine in *N*-methylpyrrolidone with two couplings of 30 minutes each.

Peptides were cleaved off resin using 500 μL of cleavage solution [95% trifluoroacetic acid (TFA), 2.5% water, and 2.5% triisopropylsilane] with shaking for 1 hour before immediate precipitation in 45 mL of ice-cold 1:1 diethyl ether:hexanes. Precipitated peptides were pelleted, the supernatants were decanted, and the pellets were allowed to dry at room temperature overnight. Crude peptides were solubilized in 1:1:1 DMSO:acetonitrile:water with 0.1% TFA and purified by high-performance liquid chromatography on an Agilent Pursuit 5 C18 column (5 mm bead size, 150 × 21.2 mm) using an Agilent PrepStar 218 series preparative high-performance liquid chromatography suite. The mobile phase consisted of water (0.1% TFA) and an increasing gradient of acetonitrile (0.1% TFA) from 20% to 80%. Solvent was removed under reduced atmosphere using a GeneVac EZ-2 4.0 Personal Evaporator (SP scientific, RRID: SCR_017367) and 50 mmol/L DMSO stocks were made based on the gross peptide mass. Purity was confirmed by LC/MS as detailed below. Stocks were stored at −20°C. Covalent modification of peptides with sotorasib was done in solution with previously purified peptides. A volume of 100 μL of 50 mmol/L peptide solution was added to 100 μL of 100 mmol/L sotorasib and 15 μL neat diisopropylethylamine in 1.5-mL Eppendorf tubes. Reaction mixtures were rotated for 1 hour at room temperature, and reactions were stopped by the addition of 20 μL TFA. Products were then purified as described above. Generated peptides were used in MHC I complex generation.

LC/MS analysis of synthetic peptides

LC/MS analysis of synthetic peptides was performed as previously described (5). An aliquot (1 μL) of the peptide solution (typically 10 mmol/L) was diluted with 100 μL 1:1 acetonitrile:water (0.1% formic acid). The diluted solution (1 μL) was injected onto a Waters Acquity UPLC BEH C18 1.7 μm column (RRID: SCR_025677) and eluted with a linear gradient of 5% to 95% acetonitrile/water (+0.1% formic acid) over 3.0 minutes. Chromatograms were recorded with a UV detector set at 254 nm and a time-of-flight mass spectrometer (Waters Xevo G2-XS, RRID: SCR_020885).

Bioconjugation of P1B7 IgG

p-SCN-Bn-Deferoxamine (B-705) and p-SCN-Bn-DOTA (B-205) were purchased from Macrocyclics and directly used for conjugation to antibody. Macropa-$(PEG)_4$-TFP was provided by Kondapa Naidu Bobba (Flavell Lab, UCSF). Chelator conjugation of P1B7 IgG was achieved using slight modifications from a previously published protocol (23–25). Briefly, to 1 mL of P1B7 IgG (2 mg/mL, 1 eq) in PBS, 0.1 mol/L $NaHCO_3$ (200 μL, pH = 9) was added to adjust the pH of the reaction mixture. p-SCN-DFO (0.040 mg, 4 eq)/ p-SCN-Bn-DOTA (0.548 mg, 60 eq)/Macropa-PEG_4-TFP (0.102 mg, 7.5 eq) dissolved in DMSO was added to the reaction mixture. The reaction was incubated in an incubator shaker for 2 hours at 37°C. After 2 hours, the reaction mixture was purified using a G25 desalting column (Cytiva, 28918007). The purified product was collected in 500-μL fractions and analyzed on a NanoDrop spectrophotometer (ND-1000 Spectrophotometer, RRID: SCR_016517) to calculate the concentration (mg/mL) for each fraction. The fractions were stored at 4°C until further use.

^{89}Zr radiolabeling of P1B7 IgG

$^{89}Zr(oxalate)_4$ (20 mCi) was received from 3D Imaging, LLC. A 0.1 mol/L Na_2CO_3 solution (50 μL, pH = 9) was added to $^{89}Zr(oxalate)_4$ (10 mCi, 50 μL) to adjust the pH to 7. Radiolabeling was performed by adding 5 mCi (50 μL) ^{89}Zr to a reaction mixture of P1B7 IgG (471 μg, 250 μL, 1.884 mg/mL) in PBS buffer (pH = 7) at 37°C for 1 hour. Radiolabeling was monitored by radio iTLC using method A. After 1 hour, the reaction mixture was diluted by adding 500 μL PBS and purified using a PD10 desalting column (Cytiva, GE17-0851-01). The isolated ^{89}Zr-P1B7 IgG (4.56 mCi) was assessed for its purity using radio iTLC (method A). Purity >99%, RCY = 91%.

^{177}Lu radiolabeling of P1B7 IgG

$^{177}LuCl_3$ 75.2 mCi was received from Oak Ridge National Laboratory (RRID: SCR_011475). Radiolabeling was performed by adding 15 mCi (50 μL) ^{177}Lu to a reaction mixture of P1B7 IgG (600 μg, 221 μL, 2.715 mg/mL) in NH_4OAc buffer (0.2 mol/L, pH = 5.5) at 37°C for 1 hour. Radiolabeling was monitored by radio iTLC using method A. After 1 hour, the reaction mixture was purified using a PD10 desalting column (GE17-0851-01). The isolated ^{177}Lu-P1B7 IgG (14.25 mCi) was assessed for its purity using radio iTLC (method A). Purity >99%, RCY = 95%.

^{225}Ac radiolabeling of P1B7 IgG

$^{225}Ac(NO_3)_3$ (1 mCi) was received from Oak Ridge National Laboratory (RRID: SCR_011475) in solid form. A 0.2 mol/L HCl solution (100 μL) was added to the mother vial to dissolve $^{225}Ac(NO_3)_3$. Radiolabeling was performed by adding 45 μCi (10 μL) ^{225}Ac to a reaction mixture of P1B7 IgG (100 μg, 100 μL, 1.001 mg/mL) in NH_4OAc buffer (200 μL, 0.2 mol/L, pH = 5.5) and L-ascorbic acid (50 μL, 150 mg/mL) at 37°C for 1 hour. Radiolabeling was monitored by radio iTLC using method A. After 1 hour, the reaction mixture was diluted by adding 200 μL PBS and purified using an Ultracel 30K centrifugal filtration tube (Millipore) by centrifuging at 10,400 rpm for 5 minutes. PBS (500 μL) was added to the product and centrifuged at 10,400 rpm for an additional 5 minutes. The isolated ^{225}Ac-P1B7 IgG (35 μCi) was assessed for its purity using radio iTLC (method A). Purity >99%, RCY = 77%.

PET/CT imaging with ^{89}Zr-P1B7 IgG

Mice were treated or untreated with 100 mg/kg sotorasib starting a day before imaging via oral gavage. A dose of 110 to 120 μCi of ^{89}Zr-P1B7 IgG (11.77 μg IgG/mouse) in saline was intravenously injected via tail vein in mice treated or untreated with 100 mg/kg sotorasib bearing either UMUC3 (RRID: CVCL_1783) or H358 (RRID: CVCL_1559) tumors (n = 4/arm). Mice were imaged on a micro PET/CT scanner (Inveon, Siemens Healthcare) at 2, 4, 6, 24, 48, 72, 96, and 120 hours after injection. The static scan included 20 minutes of PET data acquisition followed by a 10 minutes CT acquisition.

Amide (amide.sourceforge.net, RRID: SCR_005940) was used to analyze the PET/CT scans. Its automated SUV calculation tool was used by entering decay-corrected injected activity and the animal weight. For each volume of interest, a spherical VOI (2–3 mm diameter) was drawn and SUV was calculated by VOI statistics.

Biodistribution studies with ^{89}Zr-P1B7 IgG

A dose of 110 to 120 μCi/mouse of ^{89}Zr-P1B7 IgG was intravenously injected via tail vein in mice treated or untreated with 100 mg/kg sotorasib bearing either UMUC3 (RRID: CVCL_1783) or H358 (RRID: CVCL_1559) tumors (n = 4/arm). Mice were sacrificed 120 hours after injection and select organs were harvested. Radioactivity was counted by using a Hidex automatic gamma counter (RRID: SCR_025751), and the radioactivity associated with each organ was expressed as % ID/g.

Antitumor assessment studies with ^{177}Lu-P1B7 IgG

The study was split into four arms ($n = 8$/arm): saline, sotorasib (30 or 100 mg/kg), ^{177}Lu-P1B7 IgG (~400 or ~650 μCi/mouse, dosed on day 1 and 10 or day 1 and 7, respectively), and sotorasib (30 or 100 mg/kg) and ^{177}Lu-P1B7 IgG (~400 or ~650 μCi/mouse, dosed on day 1 and 10 or day 1 and 7, respectively) arm. Mice received either saline or sotorasib (30 or 100 mg/kg) via oral gavage starting on day 0 and once a day thereafter until the end of dosing on either day 7 or 10. Mice receiving the ^{177}Lu-P1B7 IgG in saline were dosed via tail vein injection on day 1 and 7 or day 1 and 10. Mice were monitored for tumor sizes and body weight every other day. Mice were euthanized if they reached the experimental end point of tumor volume >2,000 mm^3 or ≥20% loss in mouse body weight. Total protein dose was 16.2 μg IgG/mouse.

Antitumor assessment studies with ^{225}Ac-P1B7 IgG

The study was split into four arms ($n = 8$/arm): saline, sotorasib/adagrasib (30 or 100 mg/kg), ^{225}Ac-P1B7 IgG (~0.5 or ~0.6 μCi/mouse, dosed on day 1 or on day 1 and 10), and sotorasib/adagrasib (30 or 100 mg/kg) and ^{225}Ac-P1B7 IgG (~0.5 or ~0.6 μCi/mouse, dosed on day 1 or on day 1 and 10) arm. Mice received either saline or sotorasib/adagrasib (30 or 100 mg/kg) via oral gavage starting on day 0 and once a day thereafter until the end of dosing on either day 7 or 10. Mice receiving the ^{225}Ac-P1B7 IgG were given ~0.5 or ~0.6 μCi dissolved in saline via tail vein injection on day 1 or on day 1 and 10. Mice were monitored for tumor sizes and body weight every other day. Mice were euthanized if they reached the experimental end point of tumor volume >2,000 mm^3 or ≥20% loss in mouse body weight. Total protein dose was 1.1 μg IgG/mouse.

Cryo-EM sample preparation and data collection

Samples of P1B7 at 26 μmol/L and HLA–A*03:01–V7–sotorasib complex at 29 μmol/L were thawed and mixed at a 1:2.5 ratio. Fifty microliters were injected and purified by SEC with a Superdex 200 increase 3.2/300 column on an ÅKTA pure (Cytiva, RRID: SCR_023461) in a buffer containing 20 mmol/L HEPES pH 7.5, 100 mmol/L KCl. The peak fraction was collected and diluted to 0.1 μmol/L. Gold holey carbon 1.2/1.3 400 mesh grids (Quantifoil) were glow discharged at 15 mA for 30 seconds and coated with graphene oxide (GO) flakes as described previously (26). Three microliters of P1B7-HLA-A*03:01-V7-510 sample were added to the GO-grids, blotted for 6 seconds with blot force zero after a wait time of 30 seconds at 4°C and 100% humidity in a FEI Vitrobot Mark IV (Thermo Fisher Scientific, RRID: SCR_025773), and plunged into liquid ethane.

A total of 3,795 movies were collected with a 3 by 3 image-shift collection strategy at a nominal magnification of 105,000× (physical pixel size: 0.835Å/pixel) on a Titan Krios G2 (Thermo Fisher Scientific, RRID: SCR_025781) equipped with a K3 camera and a BioQuantum energy filter (GATAN, RRID: SCR_019937) with a 10 eV energy slit. The collection dose rate was 16 electrons/pixel/second for a total dose of 45.8 electrons/Å^2. Defocus range was −0.7 to −2.4 μm. The collection was performed with semi-automated scripts in SerialEM (RRID: SCR_017293; ref. 27).

Cryo-EM image processing and model building

Using MotionCor2 (RRID: SCR_016499), 3,795 movies were motion corrected and dose-weighted. The dose-weighted summed micrographs were imported into CryoSPARC(v3.2.0, RRID: SCR_016501; refs. 28, 29). Contrast-transfer function (CTF) parameters and max CTF fit resolution were estimated for each micrograph using patchCTF in CryoSPARC (v3.2.0, RRID: SCR_016501). Micrographs with CTF fit better than 6 Å were selected and subsequently manually curated. Initial particle picking was carried out with a blob picker, followed by 2D classification to generate templates. Consequent template-based particle picking resulted in 760,360 particles, which were sorted via multiple rounds of 3D classification. Iterative rounds of *ab initio* reconstruction and heterogeneous refinement yielded a stack of 288,405 particles. Non-uniform refinement of these particles lead to a 3.1 Å cryo-EM map with a final applied b-factor of −141.

The P1B7 starting structure was based on a crystal structure of a human IgG (PDB: 1MCO; sequence identity 84.17%) for the variable domain and the crystal structure of HPV L1–directed Fab (PDB: 7MU4; sequencing identity 72.59%) for the constant domain. The MHC heavy chain and B2m from the crystal structure of HLA A*03:01 (PDB: 7UC5) was fit into the density separately and then all were fit as rigid bodies in ChimeraX (RRID: SCR_015872) into the cryo-EM map. These IgG structures contained CDR loops mutated to GS linkers. Both the Fab region and MHC complex were flexibly fit into the cryo-EM density together using Rosetta (RRID: SCR_015701) FastRelax mover in torsion space (30). Next, the CDR loops were mutated to the correct residues in COOT (RRID: SCR_014222; ref. 31) and then rebuilt into the density using the iterative fragment sampling Rosetta script (RRID: SCR_015701) to make 1,920 different models of possible loop conformations (32). The top 15 of each loop (based on lowest energies and fit) were manually inspected in ChimeraX (RRID: SCR_015872), and the top designs from manual examination were selected (29). The P1B7–V7–sotorasib–A*03:01 complex was further refined in Isolde 1.0 (RRID: SCR_025577) through a plugin for UCSF ChimeraX (RRID: SCR_015872; ref. 33). At this point, iterative rounds of Isolde, Rosetta FastRelax (RRID: SCR_015701), and Realspace Refine in COOT (RRID: SCR_014222) and manual examination were used to improve the fitting of the model while keeping the geometries realistic. The final structure was validated using phenix.validation_cryoem (RRID: SCR_014224; ref. 34). The molecular interfaces and bond formation were analyzed using the PISA web server (RRID: SCR_015749; ref. 35). Visualization and figure generation was done in ChimeraX (RRID: SCR_015872; ref. 29).

Data availability

The three-dimensional cryo-EM density map has been deposited in the Electron Microscopy Data Bank (EMDB) under accession number EMD-42151. Atomic coordinates for the atomic model have been deposited in the RCSB Protein Data Bank (PDB) under accession number 8UDR. Any additional information required to reanalyze the data reported in this article is available from the lead contact upon request.

Results

PET shows sotorasib-dependent tumoral uptake of ^{89}Zr-P1B7 IgG in mouse cancer models

P1B7 is an antibody that binds with high affinity to sotorasib-modified, KRAS G12C–derived MHC I complexes but not cognate MHC I complexes lacking sotorasib modification (5). P1B7 also shows cross-reactivity, binding multiple MHC I alleles bearing sotorasib-modified KRAS G12C peptides with high affinity, including the common alleles A*02:01 and A*03:01 (Supplementary Fig. S1). To demonstrate antigen display on tumors *in vivo* and to confirm that P1B7 localizes to the tumor microenvironment upon sotorasib

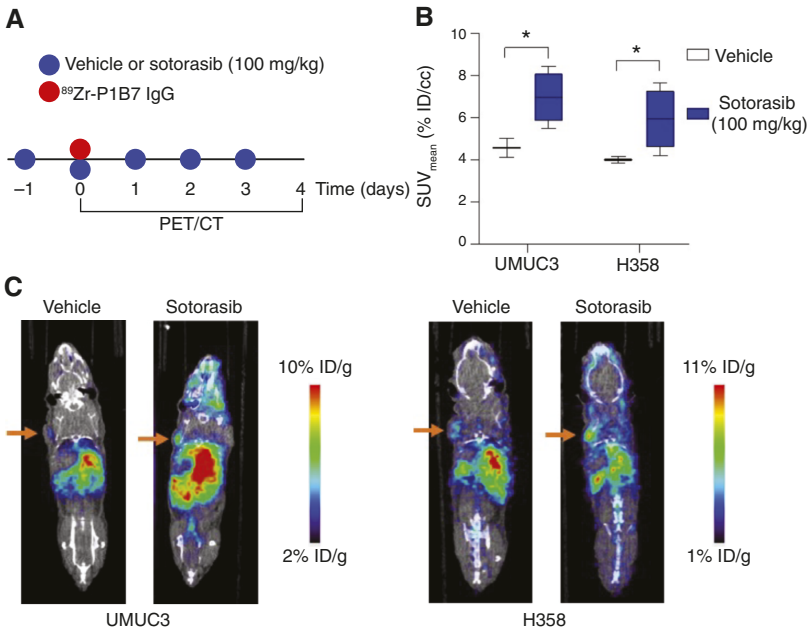

Figure 1.

PET/CT study with ^{89}Zr-P1B7 IgG shows sotorasib treatment augments tumoral uptake of the radiotracer. **A,** Dosing schema for the study to evaluate the impact of sotorasib treatment on ^{89}Zr-P1B7 IgG biodistribution in mice bearing UMUC3 and H358 subcutaneous xenografts. Tumor-bearing male nu/nu mice (n = 4/arm) were treated with vehicle or sotorasib (100 mg/kg) via oral gavage daily, starting at day 1. Eighteen hours after the first dose, the mice received an i.v. injection of ^{89}Zr-P1B7 IgG (day 0). PET/CT studies were conducted at various time points after injection of ^{89}Zr-P1B7 IgG. **B,** Mean tumoral standardized uptakes values (SUV_{mean}) showing the level of uptake of ^{89}Zr-P1B7 IgG in UMUC3 or H358 xenografts at 48 hours after injection. Sotorasib treatment significantly increases tumor uptake of ^{89}Zr-P1B7 IgG in both UMUC3 and H358 xenografts. *, $P < 0.01$; unpaired two-tailed Student t test. All data are represented via box and whisker plots, indicating mean ± SD. **C,** Representative coronal PET/CT images showing the biodistribution of ^{89}Zr-P1B7 IgG in mice bearing UMUC3 and H358 subcutaneous xenografts. Arrows, location of the tumor on the left shoulder. Images were acquired at 48 hours after ^{89}Zr-P1B7 IgG injection. ^{89}Zr-P1B7 IgG localization is represented by a heatmap of percent injected dose per gram (% ID/g).

treatment, P1B7 IgG was radiolabeled with Zr-89 (zirconium-89) for PET using established methods (Supplementary Fig. S1; ref. 36). Mice (n = 4/arm) bearing either UMUC3 (human bladder carcinoma, *KRAS G12C*, A*02:01) or H358 (human non–small cell lung carcinoma, *KRAS G12C*, A*03:01) subcutaneous xenografts were treated with vehicle (saline) or sotorasib (100 mg/kg, oral gavage) and coadministered ^{89}Zr-P1B7 (110–120 μCi/mouse, IV) according to the schema in **Fig. 1A**. The first dose of sotorasib preceded ^{89}Zr-P1B7 by 24 hours to ensure that antigen was present at the time of radiotracer injection. PET/CT acquisitions at 48 hours after injection showed higher radiotracer uptake in the tumors of mice treated with sotorasib compared with those receiving vehicle (**Fig. 1B** and **C**). Postmortem analysis of radioactivity in tumor, blood, and dissected normal tissues showed that sotorasib treatment only impacted the biodistribution of ^{89}Zr-P1B7 IgG in tumors (**Fig. 1B**; Supplementary Fig. S2).

Radioligand therapy with ^{225}Ac-P1B7 IgG displays sotorasib-dependent antitumor activity

Given the low abundance of peptide MHC I complexes, we first armed P1B7 with Ac-225, a highly potent α-emitter (18). We chose to radiolabel the IgG form of P1B7 as we expected the extended circulation time of the antibody and its high potency would maximize tumor exposure. Moreover, recent phase II data from patients with metastatic castration-resistant prostate cancer have shown that an ^{225}Ac-labeled IgG (J591, antiprostate-specific membrane antigen) can impart clinical responses with minimal bone marrow suppression despite a long circulation time (37).

P1B7 IgG was functionalized with the chelator Macropa and radiolabeled with Ac-225 using an established protocol (Supplementary Fig. S1; refs. 38, 39). Despite having the *KRAS G12C* allele, UMUC3 is relatively insensitive to sotorasib monotherapy. On this basis, we established subcutaneous xenografts in mice to test if ^{225}Ac-P1B7 treatment conferred antitumor effects specifically when coadministered with sotorasib. Tumor-bearing mice (n = 8/arm) received (i) saline, (ii) sotorasib (100 mg/kg), (iii) ^{225}Ac-P1B7 IgG (0.5 μCi/dose), or (iv) sotorasib (100 mg/kg) with ^{225}Ac-P1B7 IgG (0.5 μCi/dose) according to the treatment scheme outlined in **Fig. 2A**. Following cessation of treatment on day 10, xenografts were followed for a total of 28 days (**Fig. 2B**). In order to evaluate significant changes in tumor volumes among treatment arms over the full duration of the study, we utilized linear mixed models as described in Materials and Methods. The statistical analysis showed that coadministering sotorasib with ^{225}Ac-P1B7 significantly inhibited tumor growth compared with treatment arms receiving vehicle, sotorasib, or ^{225}Ac-P1B7 alone ($P < 0.001$). The comparatively milder antitumor effects of ^{225}Ac-P1B7 monotherapy are likely attributable to nonspecific background tumor accumulation observed on the PET/CT study (**Fig. 1**), which may be driven by the enhanced permeability and retention effect (40, 41). An additional study utilizing a reduced dose of sotorasib (30 mg/kg) was carried out (Supplementary Fig. S3). Despite this

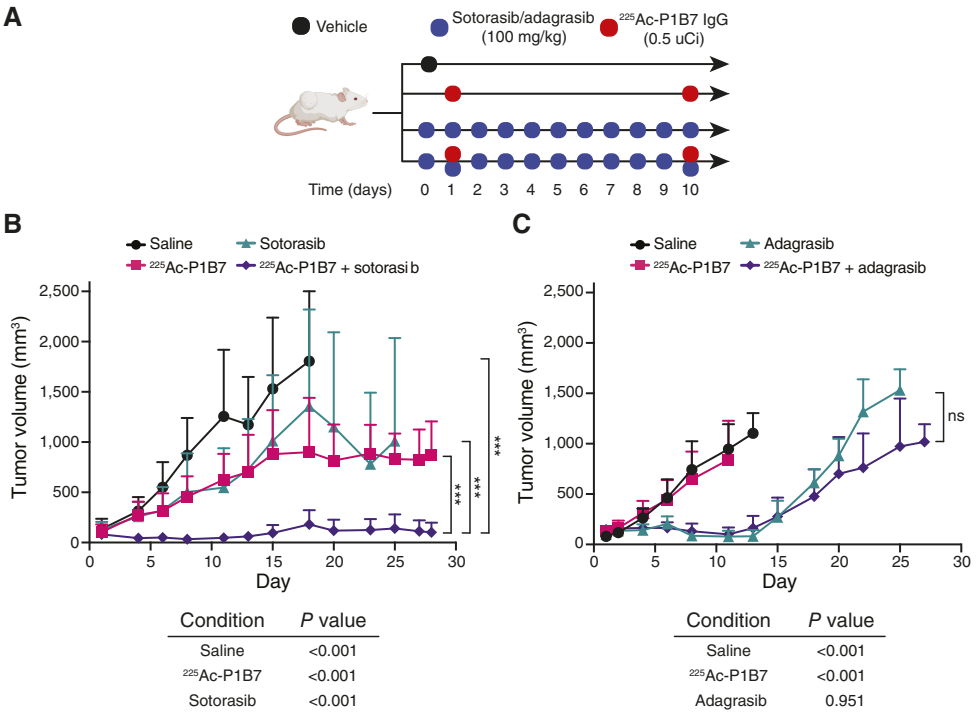

Figure 2.

The antitumor effects of ^{225}Ac-P1B7 IgG are potentiated by treatment of tumors with sotorasib but not adagrasib. **A,** Schema showing the treatment arms and dosing schedule for the antitumor assessment study of ^{225}Ac-P1B7 IgG in mice bearing subcutaneous UMUC3 xenografts. Tumor-bearing male nu/nu mice (n = 8/arm) received KRAS G12C inhibitor (sotorasib or adagrasib, 100 mg/kg) via oral gavage daily, starting on day 0. Eighteen hours after the first inhibitor dose, mice received ^{225}Ac-P1B7 IgG (0.5 μCi) intravenously. Inhibitor was dosed daily until day 10 when a second dose of ^{225}Ac-P1B7 IgG (0.5 μCi) was given and all subsequent treatment ceased. **B,** Tumor volume data from each treatment arm of sotorasib study represented as mean + SD. Coadministration of sotorasib with ^{225}Ac-P1B7 resulted in significantly reduced tumor burden when compared with all other treatment arms (linear mixed model). ***, $P < 0.001$. P values are shown for cotreatment against all other arms. **C,** Tumor volume data from each treatment arm of adagrasib study are represented as mean + SD. Coadministration of ^{225}Ac-P1B7 with adagrasib did not further suppress tumor growth compared with treatment with adagrasib alone (linear mixed model; $P = 0.951$). All data are represented as mean + SD. P values are shown for cotreatment against all other arms. ns, nonsignificant. (**A,** Created with BioRender.com.)

reduction in sotorasib dose and treatment with only a single dose of ^{225}Ac-P1B7 (0.6 μCi), the combination therapy remained efficacious, resulting in a statistically significant ($P < 0.001$) reduction in tumor burden compared with all other treatment arms (Supplementary Fig. S3).

To test the specificity of ^{225}Ac-P1B7 IgG, a separate cohort of mice bearing UMUC3 tumors was treated with the structurally distinct KRAS G12C inhibitor adagrasib (4). Mice (n = 8/arm) received (i) saline, (ii) adagrasib (100 mg/kg), (iii) ^{225}Ac-P1B7 IgG (0.5 μCi/dose), or (iv) adagrasib (100 mg/kg) with ^{225}Ac-P1B7 IgG (0.5 μCi/dose) according to the treatment schedule outlined in **Fig. 2A**. Following cessation of all treatment on day 10, xenografts were followed for a total of 28 days. Due to its increased potency, adagrasib treatment suppressed tumor growth to a greater extent than the same dose of sotorasib (**Fig. 2C**). However, cotreating mice with adagrasib and ^{225}Ac-P1B7 IgG did not further inhibit tumor growth when compared with treatment with adagrasib alone ($P = 0.951$). Due to the potency of adagrasib monotherapy, these two conditions both show strong tumor suppression during the period when adagrasib was administered, but xenografts treated with either adagrasib condition rapidly rebounded after cessation of inhibitor treatment on day 10, in stark contrast to treatment with ^{225}Ac-P1B7 IgG and sotorasib, which was protective through the entire length of the study (**Fig. 2B**). This result is consistent with P1B7's specificity for sotorasib-derived antigens.

^{177}Lu-P1B7 IgG inhibits tumor growth by targeting sotorasib-labeled MHC I complexes

We next evaluated P1B7 IgG labeled with Lu-177 to determine if a radioisotope with low linear energy transfer would confer antitumor effects. ^{177}Lu-P1B7 IgG was synthesized and characterized according to previously established methods (Supplementary Fig. S1; refs. 23, 36). Mice bearing subcutaneous UMUC3 xenografts (n = 8/arm) received (i) saline, (ii) sotorasib (100 mg/kg), (iii) ^{177}Lu-P1B7 IgG (400 μCi/dose), or (iv) sotorasib (100 mg/kg) and ^{177}Lu-P1B7 IgG (400 μCi/dose) according to the dosing scheme outlined in **Fig. 3A**. Following cessation of treatment on day 10, xenografts were followed for a total of 28 days. Treating mice with either sotorasib or ^{177}Lu-P1B7 IgG alone did not inhibit tumor growth (**Fig. 3B**). However, cotreatment of ^{177}Lu-P1B7 IgG with sotorasib resulted in significant inhibition of tumor growth compared with the other treatment arms ($P < 0.001$; **Fig. 3B**; Supplementary Fig. S4).

We next tested if ^{177}Lu-P1B7 could inhibit the growth of tumors exposed to a lower dose of sotorasib. A cohort of mice bearing UMUC3 tumors as treated with (i) saline, (ii) sotorasib (30 mg/kg), (iii) ^{177}Lu-P1B7 IgG (650 μCi/dose), or (iv) sotorasib (30 mg/kg)

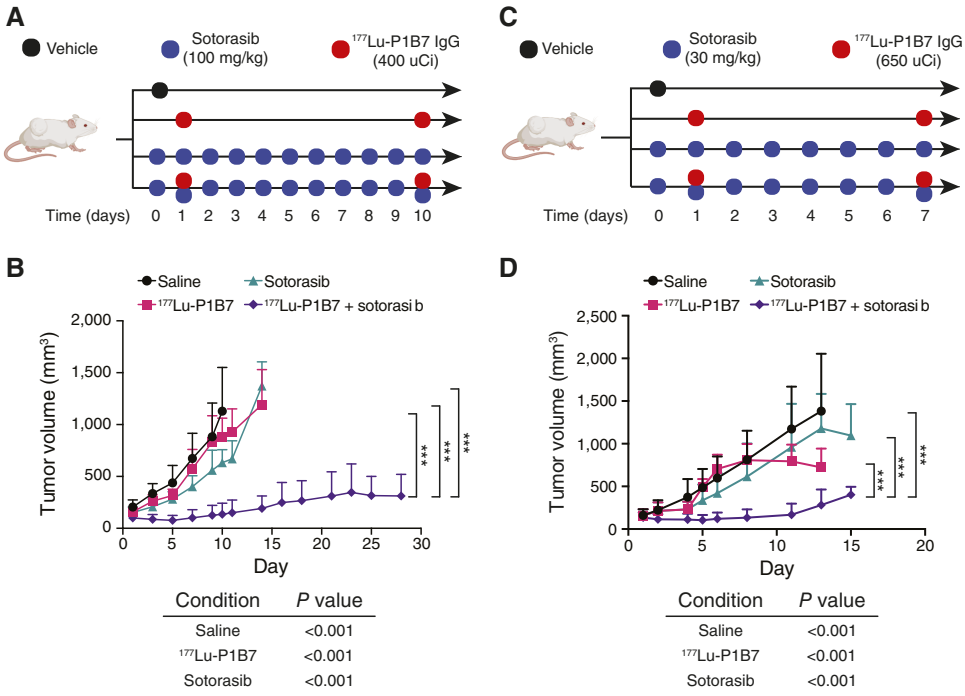

Figure 3.

The antitumor effects of ^{177}Lu-P1B7 IgG are sotorasib-dependent. **A,** Schema showing the treatment arms and dosing schedule for antitumor assessment study of ^{177}Lu-P1B7 IgG in mice bearing UMUC3 xenografts. Tumor-bearing male nu/nu mice (n = 8/arm) received sotorasib (100 mg/kg) via oral gavage daily for 11 days, starting at day 0. Eighteen hours after the first dose and on day 10, mice received ^{177}Lu-P1B7 IgG (400 μCi) intravenously. **B,** Plot showing the impact of treatments on UMUC3 xenograft volume. All data are represented as mean + SD. Cotreatment with ^{177}Lu-P1B7 IgG and sotorasib resulted in significantly reduced tumor burden when compared with all other treatment arms (linear mixed model). ***, $P < 0.001$. P values are shown for cotreatment against all other arms. **C,** Schema showing the treatment arms and dosing schedule for antitumor assessment study of ^{177}Lu-P1B7 IgG in mice bearing UMUC3 xenografts. Tumor-bearing male nu/nu mice (n = 7/arm) received sotorasib (30 mg/kg) via oral gavage daily for 8 days, starting at day 0. Eighteen hours after the first dose and on day 7, mice received ^{177}Lu-P1B7 IgG (650 μCi) intravenously. **D,** Plot showing the impact of treatments on UMUC3 xenograft volume. All data are represented as mean + SD. Cotreatment of mice with sotorasib and ^{177}Lu-P1B7 IgG resulted in significantly reduced tumor burden when compared with all other treatment arms (linear mixed model). ***, $P < 0.001$. P values are shown for cotreatment against all other arms. (**A** and **C,** Created with BioRender.com.)

and ^{177}Lu-P1B7 IgG (650 μCi/dose) according to the dosing scheme outlined in **Fig. 3C**. Following cessation of treatment on day 7, mice were followed for a total of 18 days. As expected, treatment with sotorasib or ^{177}Lu-P1B7 IgG alone was ineffective, but combination therapy significantly inhibited tumor growth compared with the other treatment arms ($P < 0.001$; **Fig. 3D**; Supplementary Fig. S4).

To evaluate the efficacy of the ^{177}Lu-P1B7 RLT in another biological replicate, we carried out an antitumor assessment study in male nu/nu mice bearing subcutaneous H358 xenografts using the study design detailed in Supplementary Fig. S5. Combination therapy with sotorasib and ^{177}Lu-P1B7 IgG significantly inhibited tumor growth compared with all other treatment arms ($P < 0.001$), although the slower overall growth rate and greater sotorasib sensitivity of H358 xenografts resulted in less well-resolved cohorts relative to the UMUC3 xenograft model (Supplementary Fig. S5B). Collectively, these results demonstrate that sotorasib-derived MHC I complexes are an appropriate target for RLT and that cotreatment of a P1B7 RLT with sotorasib results in superior therapeutic benefit to treatment with inhibitor alone.

Structural characterization of the P1B7:V7–sotorasib A*03:01 MHC I complex with cryo-EM

Having demonstrated P1B7's efficacy as a RLT, we next sought to understand its binding mode through structural elucidation with cryo-EM. P1B7 shows exquisite specificity for the inhibitor-modified MHC I complex (Fab K_D = 15 nmol/L) over the cognate WT MHC I complex (binding not detected, Fab K_D > 1 μmol/L), implying that the sotorasib moiety is critical for its binding (5). To better understand the molecular determinants of P1B7's specificity toward the V7–sotorasib A*03:01 MHC I complex, we solved a 3.1 Å cryo-EM structure of the complex (**Fig. 4**; Supplementary Figs. S6–S9; Supplementary Table S1). The resulting structure captures key elements of our therapeutic design approach. P1B7 binds the complex at the interface of the MHC I protein and the presented, sotorasib-modified peptide, much like a T-cell receptor (TCR; **Fig. 4A**). The sotorasib-modified KRAS G12C peptide V7 [VVVGAC(Sotorasib)GVGK] binds to the A*03:01 MHC I complex via a canonical binding pose, positioning valine-7 and valine-8 as N-terminal anchors in the A and B pockets and lysine-16 as a C-terminal anchor in the F pocket (**Fig. 4B**; ref. 42). This binding pose is consistent with the crystal structure of the WT V7 peptide in A*03:01, indicating that the drug modification does not significantly shift the binding of the peptide backbone to the A*03:01 MHC I complex (Supplementary Fig. S8A–S8C; ref. 43). This positioning of the cargo peptide is similar to what is typically observed in MHC I structures, corroborating a large body of work showing that post-translational modifications on peptides are well-tolerated in MHC I complexes (44, 45). There is a clear coulombic potential density branching from the

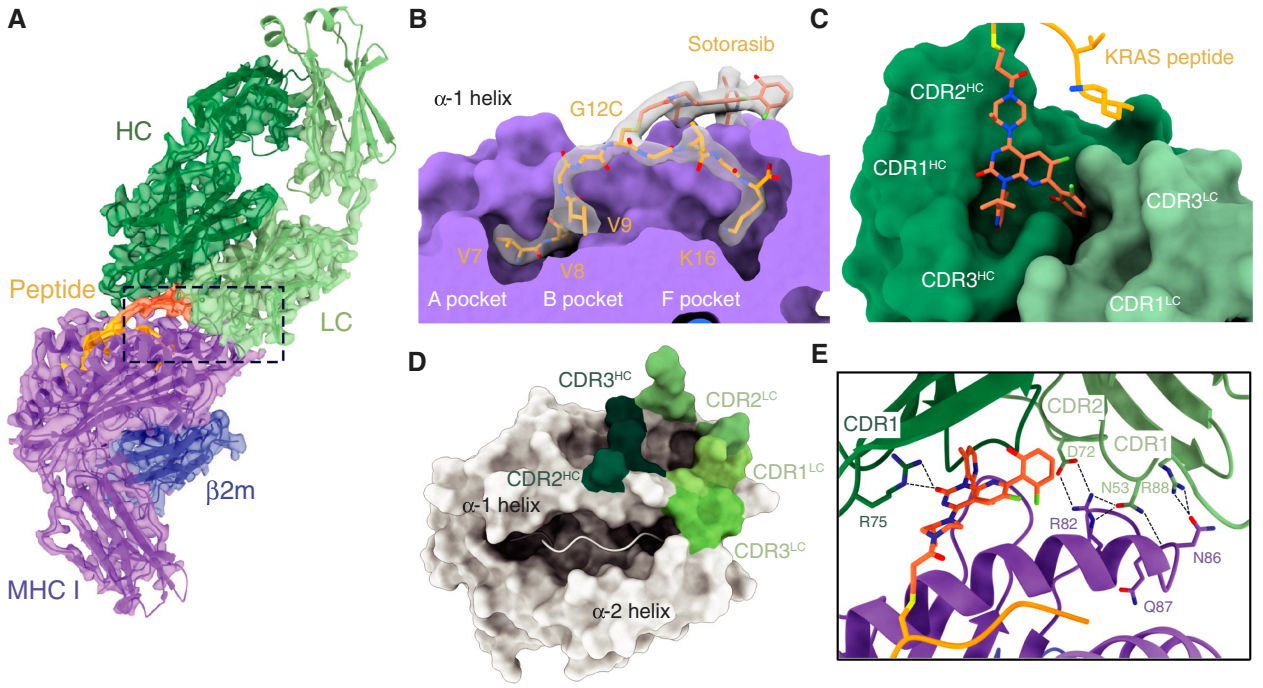

Figure 4.

Cryo-EM structure of P1B7 bound to V7–sotorasib A*03:01 MHC I complex (PDB 8UDR). **A,** A 3.1-Å cryo-EM map and resulting structural model of P1B7 bound to the A*03:01 MHC I complex presenting the covalently modified KRAS peptide V7–sotorasib [VVVGAC(Sotorasib)GVGK]. **B,** Zoomed-in view of V7–sotorasib peptide superimposed with cryo-EM density illustrating the MHC I protein (purple) binding the V7–sotorasib peptide (orange) via a canonical binding pose, using N-terminal (V7 and V8) and C-terminal (K16) anchor residues. The sotorasib-modified cysteine side chain protrudes above the MHC I peptide binding cleft. **C,** P1B7 binds sotorasib (orange) at the interface of its heavy (dark green) and light chain (light green) via two small pockets that accommodate the 2-fluoro-6-hydroxyphenyl and 2-isoproyl-4-methyl- pyridin-3-yl groups of sotorasib. Additionally, sotorasib is hydrogen bonded with R75 of the P1B7 heavy chain. **D,** Top view of the A*03:01 MHC I complex (surface representation) shown in gray, with P1B7 contacting residues colored by corresponding CDR loops. **E,** Zoomed-in view of P1B7 and MHC interface (dashed black box in **A**) highlighting intermolecular polar interactions between the CDR loops of P1B7 and the MHC α-helix I. Additionally, sotorasib is hydrogen bonded with R75 of the P1B7 heavy chain CDR1 loop.

middle of the peptide, which is well accounted for by the covalently attached sotorasib, indicating that the drug modification is pointed up toward solvent where it is accessible for binding by P1B7. The drug is nestled in a shallow pocket at the interface between the variable domains of the heavy and light chains of P1B7 using the residues of complementarity-determining regions CDR2 (Y73, R75, and Y79) and CDR3 (P127) of its heavy chain and CDR3 (H113 and T118) of its light chain (**Fig. 4C**). P1B7 directly contacts the presenting MHC I protein predominantly at its α-1 helix (**Fig. 4D**). The P1B7–MHC I binding is driven by polar interactions through the light chain CDR1 (N53 and R88) and CDR2 (D72), whereas the heavy chain CDR1 (R75) forms a hydrogen bond with the sotorasib adduct (**Fig. 4E**). The V7–sotorasib peptide accounts for approximately 38% of the buried surface area of P1B7's epitope, contributing slightly more binding surface than what is typically observed with peptides in TCR–MHC I complex structures in the RCSB Protein Data Bank (~29%; ref. 46). Particularly interesting is the positioning of P1B7 relative to the MHC I complex as it binds the complex at an angle of 30° from perpendicular, approaching from the C-terminal side of the presented peptide (**Fig. 4D**; Supplementary Fig. S8D). This is considerably different from most previously solved TCR–MHC I structures where the approach of the TCR is perpendicular to the plane of the peptide binding cleft and typically contacts the middle of the peptide cargo (Supplementary Fig. S8D and S8E; ref. 46). This unique binding pose is most similar to TCR recognition of lipid-presenting MHC I complexes (Supplementary Fig. S8E; refs. 47, 48). Compared with TCRs, which are evolutionarily selected for a standard binding pose, engineered MHC I–binding antibodies are unrestricted and more diverse in their binding approach. This is demonstrated by the comparison of P1B7's binding mode to that of R023, another antibody that binds the V7–sotorasib A*03:01 MHC I complex (49). Despite binding the same antigen, these two antibodies approach from opposite sides of the MHC I complex, although both binding angles are more extreme than what is typically observed for TCR–MHC I structures (Supplementary Fig. S9). Overall, this cryo-EM structure provides an atomic-level understanding of the binding of a sotorasib-modified KRAS peptide to the A*03:01 MHC I complex and of P1B7's recognition of this unique composite surface. This structure serves as a roadmap for structure-guided development of next-generation antibodies with optimized binding properties to haptenated peptide–MHC I complexes.

Discussion

The results of this study demonstrate that sotorasib-modified MHC I complexes can be targeted with radioligand therapeutics, offering superior antitumor effects to treatment with sotorasib alone. Using P1B7, we were able to specifically target a sotorasib-modified, KRAS G12C–derived MHC I complex in xenograft

models of *KRAS G12C* tumors. Cotreatment of ^{225}Ac-P1B7 with adagrasib, a structurally unique inhibitor of the same target protein, did not result in the same tumor-suppressive effects as cotreatment with sotorasib. These data support that the therapeutic efficacy of the combination was the result of specific binding to sotorasib-derived antigens rather than a simple additive effect of KRAS G12C inhibition and nonspecific accumulation of radiolabeled IgG in the tumor microenvironment. Critically, this approach was effective even when xenografts were treated with sublethal doses of inhibitor. Roughly half of all patients treated with sotorasib and adagrasib display innate resistance to inhibitor monotherapy despite *KRAS G12C* mutational status, and responsive patients typically develop resistance within 6 to 12 months, dramatically reducing the clinical benefit of these breakthrough therapeutics (4, 50). Despite this high rate of resistance, most patients retain the original *KRAS G12C* mutation, achieving resistance through amplification of compensatory pathways rather than mutation of the mutant cysteine used for covalent inhibition (51). Because of this conservation of mutant KRAS G12C protein expression, our approach offers the potential to not only improve the efficacy of inhibitor monotherapy but also a means to reclaim the therapeutic efficacy of sotorasib in the case of acquired and innate resistance by repurposing sotorasib as a hapten.

The somewhat unexpected finding that low abundance peptide MHC I complexes can be targeted for RLT may help to reframe the ongoing discussion about the ideal properties of an RLT target. Indeed, much of the clinical renaissance in nuclear medicine has been driven by the design choice to prioritize low molecular weight RLTs that rapidly exit the bloodstream to minimize bone marrow suppression. Committing to rapidly clearing targeting agents in turn necessitates that the protein drug target has exceptionally high expression ($>10^5$ copies per cell) and a domain evolved for high affinity interactions with ligands ($K_D \leq$ nmol/L). Relatively few targets in biology have met these criteria. Moreover, none of the high-profile targets for RLT (e.g., prostate-specific membrane antigen, fibroblast activated protein α, and carbonic anhydrase 9) are tumor specific, and on-target, off-tissue binding limits the injectable dose and can undermine the antitumor efficacy of RLTs. Interestingly, the efficacy of the P1B7 IgG-based radioligand therapies is comparable to previous work targeting CDCP1, an antigen with $\sim10^5$ copies per cell in the xenograft models tested despite the fact that individual MHC I complexes are typically presented on the order of $\sim10^1$ to 10^2 copies per cell (36, 52). We are optimistic that our data may stimulate interest in studying more tumor specific candidates, such as oncoprotein-derived MHC I complexes, regardless of their copy number per cell. Meanwhile, the emerging clinical data with Ac-225–labeled IgGs like J591 showing efficacy at tolerable doses are timely, as an IgG format may be necessary to achieve the level of tumor exposure required to confer antitumor effects against low abundance targets (37).

It has long been appreciated that MHC I complexes can bind and present noncanonical and post-translationally modified (PTM) peptides as part of the adaptive immune system, but the limits of tolerance for unique peptide presentation remain open-ended. A growing body of work has elaborated on a subset of these unique peptide–MHC I complexes—those modulated not by endogenous PTMs but by xenobiotics (5, 6, 53, 54). The comparison of our sotorasib-modified MHC I structure to the structures of other MHC I complexes in the PDB indicates that the A*03:01 complex accommodates this inhibitor-modified peptide via a standard binding pose, using the same binding mode seen in a structure of the cognate WT peptide presented by the same A*03:01 allele despite the relatively large sotorasib modification on the mutant cysteine (43). Interestingly, the same V7–sotorasib A*03:01 MHC I complex bound by a different antibody shows the sotorasib-modified cysteine residue pointing in the opposite direction, demonstrating that although the binding pose of anchor residues buried in the MHC I complex is typically conserved, the positioning of solvent-exposed side chains can be quite flexible (49). P1B7 binds this V7–sotorasib A*03:01 complex in a non-canonical manner relative to native TCR–MHC I complexes, being positioned at a considerably different angle than what is typically observed. The standard TCR–MHC I binding pose is well-conserved and previous work has indicated that changes to the binding pose can have strong effects on downstream signaling competency (55). P1B7's unique binding pose may restrict its signaling competency in T cell–based applications.

The results presented herein demonstrate the potential value of targeting these unique oncoprotein-derived, haptenated MHC I complexes with radioligand therapeutics. The cryo-EM structure suggests that these covalently modified peptides are well-tolerated by MHC I complexes and that other PTM- or covalent inhibitor–modified peptide fragments are likely capable of forming stable MHC I complexes as well. These highly unique, tumor-specific antigens could be appropriate targets for therapeutic development. Although acquired cysteines on oncoproteins are relatively rare, this approach could be applied to additional systems, such as conserved cysteines whose chemical reactivity is altered by oncogenic mutations, like in the case of third generation EGFR inhibitors that target the T790M-resistant mutant via a WT cysteine residue, or even to systems where the chemical entity is only an alkylator and not an inhibitor of enzymatic activity (56, 57). This potential flexibility in hapten character and the results presented herein suggest that this hapten-based therapeutic strategy could serve as a general, platform approach to therapeutic development.

Authors' Disclosures

P.J. Rohweder reports nonfinancial support from Hap10 Bio and grants from NIH, Innovation Ventures Philanthropy Fund, and Marcus Program in Precision Medicine Innovation during the conduct of the study, as well as nonfinancial support from Hap10 Bio outside the submitted work and a patent for University of California, San Francisco pending. B. Paolella reports personal fees from Hap10 Bio during the conduct of the study, as well as nonfinancial support from Hap10 Bio outside the submitted work. K.A. Verba reports being a shareholder of Hap10 Bio. M.J. Evans reports other support from Hap10 Bio Inc. during the conduct of the study, as well as a patent for radiolabeled antibodies targeting peptide MHC complexes and the uses thereof pending. C.S. Craik reports grants and nonfinancial support from Hap10 Bio and grants from NIH and Markus Program in Precision Medicine Innovation during the conduct of the study, as well as nonfinancial support from Hap10 Bio outside the submitted work, as well as a patent for UCSF pending. No disclosures were reported by the other authors.

Authors' Contributions

A. Pandey: Conceptualization, investigation, visualization, formal analysis, data curation, methodology, writing–original draft, writing–review and editing. **P.J. Rohweder:** Conceptualization, investigation, visualization, formal analysis, data curation, methodology, writing–original draft, writing–review and editing. **L.M. Chan:** Investigation, visualization, formal analysis, data curation, methodology, writing–original draft, writing–review and editing. **C. Ongpipattanakul:** Resources, data curation. **D.h. Chung:** Data curation, investigation. **B. Paolella:** Resources, data curation. **F.M. Quimby:** Investigation, data curation. **N. Nguyen:** Investigation, data curation. **K.A. Verba:** Conceptualization, supervision, writing–review and editing. **M.J. Evans:** Conceptualization, resources, writing–review and

editing. **C.S. Craik:** Conceptualization, resources, supervision, funding acquisition, validation, investigation, writing–original draft, project administration, writing–review and editing.

Acknowledgments

The authors acknowledge Kevan M. Shokat (UC San Francisco) and Ziyang Zhang (UC Berkeley) for their thoughtful suggestions and support and Li Zhang for her advice and help analyzing data and running statistical analyses. We acknowledge Robert R. Flavell and Kondapa Naidu Bobba for providing Macropa-$(PEG)_4$-TFP. Youngho Seo and Rebecca Shuere are acknowledged for assistance with PET/CT acquisitions, and the instrument was supported with S10OD034286. P.J. Rohweder was supported by an NIH training grant (T32 GM 064337). C.S. Craik acknowledges the Innovation Ventures Philanthropy Fund, the Marcus Program in Precision Medicine, and the NIH (P41-GM103393). The cryo-EM equipment at UCSF is partially supported by NIH grants S10OD020054, S10OD021741, and S10OD026881 and Howard Hughes Medical Institute.

Note

Supplementary data for this article are available at Cancer Research Online (http://cancerres.aacrjournals.org/).

Received July 15, 2024; revised September 11, 2024; accepted November 11, 2024; published first December 10, 2024.

References

1. Prior IA, Hood FE, Hartley JL. The frequency of ras mutations in cancer. Cancer Res 2020;80:2969–74.
2. Zehir A, Benayed R, Shah RH, Syed A, Middha S, Kim HR, et al. Mutational landscape of metastatic cancer revealed from prospective clinical sequencing of 10,000 patients. Nat Med 2017;23:703–13.
3. Skoulidis F, Li BT, Dy GK, Price TJ, Falchook GS, Wolf J, et al. Sotorasib for lung cancers with KRAS p.G12C mutation. N Engl J Med 2021;384:2371–81.
4. Jänne PA, Riely GJ, Gadgeel SM, Heist RS, Ou S-HI, Pacheco JM, et al. Adagrasib in non–small-cell lung cancer harboring a $KRAS^{G12C}$ mutation. N Engl J Med 2022;387:120–31.
5. Zhang Z, Rohweder PJ, Ongpipattanakul C, Basu K, Bohn M-F, Dugan EJ, et al. A covalent inhibitor of K-Ras(G12C) induces MHC class I presentation of haptenated peptide neoepitopes targetable by immunotherapy. Cancer Cell 2022;40:1060–9.e7.
6. Hattori T, Maso L, Araki KY, Koide A, Hayman J, Akkapeddi P, et al. Creating MHC-restricted neoantigens with covalent inhibitors that can be targeted by immune therapy. Cancer Discov 2023;13:132–45.
7. Chang AY, Dao T, Gejman RS, Jarvis CA, Scott A, Dubrovsky L, et al. A therapeutic T cell receptor mimic antibody targets tumor-associated PRAME peptide/HLA-I antigens. J Clin Invest 2017;127:2705–18.
8. Dao T, Yan S, Veomett N, Pankov D, Zhou L, Korontsvit T, et al. Targeting the intracellular WT1 oncogene product with a therapeutic human antibody. Sci Transl Med 2013;5:176ra33.
9. Hsiue EH-C, Wright KM, Douglass J, Hwang MS, Mog BJ, Pearlman AH, et al. Targeting a neoantigen derived from a common TP53 mutation. Science 2021;371:eabc8697.
10. Li D, Bentley C, Anderson A, Wiblin S, Cleary KLS, Koustoulidou S, et al. Development of a T-cell receptor mimic antibody against wild-type p53 for cancer immunotherapy. Cancer Res 2017;77:2699–711.
11. Low L, Goh A, Koh J, Lim S, Wang C-I. Targeting mutant p53-expressing tumours with a T cell receptor-like antibody specific for a wild-type antigen. Nat Commun 2019;10:5382.
12. Weltzien HU, Dötze A, Gamerdinger K, Hellwig S, Thierse H-J. Molecular recognition of haptens by T cells: More than one way to tickle the receptor. Austin (TX): Landes Bioscience; 2013. [cited 2018 Feb 13]. Available from: https://www.ncbi.nlm.nih.gov/books/NBK6573/.
13. Martin S, Weltzien HU. T cell recognition of haptens, a molecular view. Int Arch Allergy Immunol 1994;104:10–6.
14. Morotti M, Albukhari A, Alsaadi A, Artibani M, Brenton JD, Curbishley SM, et al. Promises and challenges of adoptive T-cell therapies for solid tumours. Br J Cancer 2021;124:1759–76.
15. Edeline J, Houot R, Marabelle A, Alcantara M. CAR-T cells and BiTEs in solid tumors: challenges and perspectives. J Hematol Oncol 2021;14:65.
16. Dhatchinamoorthy K, Colbert JD, Rock KL. Cancer immune evasion through loss of MHC class I antigen presentation. Front Immunol 2021;12:636568.
17. Douglass J, Hsiue EH-C, Mog BJ, Hwang MS, DiNapoli SR, Pearlman AH, et al. Bispecific antibodies targeting mutant RAS neoantigens. Sci Immunol 2021;6:eabd5515.
18. Sgouros G, Bodei L, McDevitt MR, Nedrow JR. Radiopharmaceutical therapy in cancer: clinical advances and challenges. Nat Rev Drug Discov 2020;19:589–608.
19. Brown WS, McDonald PC, Nemirovsky O, Awrey S, Chafe SC, Schaeffer DF, et al. Overcoming adaptive resistance to KRAS and MEK inhibitors by co-targeting mTORC1/2 complexes in pancreatic cancer. Cell Rep Med 2020;1:100131.
20. Kim JM, Stroud RM, Craik CS. Rapid identification of recombinant Fabs that bind to membrane proteins. Methods 2011;55:303–9.
21. Chung DH, Kong S, Young NJ, Chuo S-W, Shiah JV, Connelly EJ, et al. Rare antibody phage isolation and discrimination (RAPID) biopanning enables identification of high-affinity antibodies against challenging targets. Commun Biol 2023;6:1036.
22. Rodenko B, Toebes M, Hadrup SR, van Esch WJE, Molenaar AM, Schumacher TNM, et al. Generation of peptide-MHC class I complexes through UV-mediated ligand exchange. Nat Protoc 2006;1:1120–32.
23. Moroz A, Wang Y-H, Sharib JM, Wei J, Zhao N, Huang Y, et al. Theranostic targeting of CUB domain containing protein 1 (CDCP1) in pancreatic cancer. Clin Cancer Res 2020;26:3608–15.
24. Bidkar AP, Wang S, Bobba KN, Chan E, Bidlingmaier S, Egusa EA, et al. Treatment of prostate cancer with CD46-targeted 225Ac alpha particle radioimmunotherapy. Clin Cancer Res 2023;29:1916–28.
25. Wang S, Li J, Hua J, Su Y, Beckford-Vera DR, Zhao W, et al. Molecular imaging of prostate cancer targeting CD46 using ImmunoPET. Clin Cancer Res 2021;27:1305–15.
26. Wang F, Liu Y, Yu Z, Li S, Feng S, Cheng Y, et al. General and robust covalently linked graphene oxide affinity grids for high-resolution cryo-EM. Proc Natl Acad Sci U S A 2020;117:24269–73.
27. Mastronarde DN. Automated electron microscope tomography using robust prediction of specimen movements. J Struct Biol 2005;152:36–51.
28. Zheng SQ, Palovcak E, Armache J-P, Verba KA, Cheng Y, Agard DA. MotionCor2: anisotropic correction of beam-induced motion for improved cryo-electron microscopy. Nat Methods 2017;14:331–2.
29. Punjani A, Rubinstein JL, Fleet DJ, Brubaker MA. cryoSPARC: algorithms for rapid unsupervised cryo-EM structure determination. Nat Methods 2017;14:290–6.
30. Wang RY-R, Song Y, Barad BA, Cheng Y, Fraser JS, DiMaio F. Automated structure refinement of macromolecular assemblies from cryo-EM maps using Rosetta. Elife 2016;5:e17219.
31. Emsley P, Lohkamp B, Scott WG, Cowtan K. Features and development of coot. Acta Crystallogr D Biol Crystallogr 2010;66:486–501.
32. Emsley P, Cowtan K. Coot: model-building tools for molecular graphics. Acta Crystallogr D Biol Crystallogr 2004;60:2126–32.
33. Croll TI. ISOLDE: a physically realistic environment for model building into low-resolution electron-density maps. Acta Crystallogr D Struct Biol 2018;74:519–30.
34. Afonine PV, Klaholz BP, Moriarty NW, Poon BK, Sobolev OV, Terwilliger TC, et al. New tools for the analysis and validation of cryo-EM maps and atomic models. Acta Crystallogr D Struct Biol 2018;74:814–40.
35. Krissinel E, Henrick K. Inference of macromolecular assemblies from crystalline state. J Mol Biol 2007;372:774–97.
36. Zhao N, Chopra S, Trepka K, Wang Y-H, Sakhamuri S, Hooshdaran N, et al. CUB domain-containing protein 1 (CDCP1) is a target for radioligand therapy in castration-resistant prostate cancer, including PSMA null disease. Clin Cancer Res 2022;28:3066–75.
37. Tagawa ST, Thomas C, Sartor AO, Sun M, Stangl-Kremser J, Bissassar M, et al. Prostate-specific membrane antigen–targeting alpha emitter via antibody delivery for metastatic castration-resistant prostate cancer: a phase I dose-escalation study of ^{225}Ac-J591. J Clin Oncol 2024;42:842–51.

38. Bobba KN, Bidkar AP, Meher N, Fong C, Wadhwa A, Dhrona S, et al. Evaluation of $^{134}Ce/^{134}La$ as a PET imaging theranostic pair for ^{225}Ac α-radiotherapeutics. J Nucl Med 2023;64:1076–82.
39. Bobba KN, Bidkar AP, Wadhwa A, Meher N, Drona S, Sorlin AM, et al. Development of CD46 targeted alpha theranostics in prostate cancer using $^{134}Ce/^{225}Ac$-Macropa-PEG_4-YS5. Theranostics 2024;14:1344–60.
40. Vilhelmsson Timmermand O, Safi M, Holmqvist B, Strand J. Evaluation of enhanced permeability effect and different linear energy transfer of radionuclides in a prostate cancer xenograft model. Am J Nucl Med Mol Imaging 2023;13:147–55.
41. Wu J. The enhanced permeability and retention (EPR) effect: the significance of the concept and methods to enhance its application. J Pers Med 2021;11:771.
42. Sidney J, Peters B, Frahm N, Brander C, Sette A. HLA class I supertypes: a revised and updated classification. BMC Immunol 2008;9:1.
43. Wright KM, DiNapoli SR, Miller MS, Aitana Azurmendi P, Zhao X, Yu Z, et al. Hydrophobic interactions dominate the recognition of a KRAS G12V neoantigen. Nat Commun 2023;14:5063.
44. Engelhard VH, Altrich-Vanlith M, Ostankovitch M, Zarling AL. Post-translational modifications of naturally processed MHC-binding epitopes. Curr Opin Immunol 2006;18:92–7.
45. Ramarathinam SH, Croft NP, Illing PT, Faridi P, Purcell AW. Employing proteomics in the study of antigen presentation: an update. Expert Rev Proteomics 2018;15:637–45.
46. Szeto C, Lobos CA, Nguyen AT, Gras S. TCR recognition of peptide-MHC-I: rule makers and breakers. Int J Mol Sci 2020;22:68.
47. Mallevaey T, Clarke AJ, Scott-Browne JP, Young MH, Roisman LC, Pellicci DG, et al. A molecular basis for NKT cell recognition of CD1d-self-antigen. Immunity 2011;34:315–26.
48. Pellicci DG, Clarke AJ, Patel O, Mallevaey T, Beddoe T, Le Nours J, et al. Recognition of β-linked self glycolipids mediated by natural killer T cell antigen receptors. Nat Immunol 2011;12:827–33.
49. Maso L, Rajak E, Bang I, Koide A, Hattori T, Neel BG, et al. Molecular basis for antibody recognition of multiple drug–peptide/MHC complexes. Proc Natl Acad Sci U S A 2024;121:e2319029121.
50. Hong DS, Fakih MG, Strickler JH, Desai J, Durm GA, Shapiro GI, et al. $KRAS^{G12C}$ inhibition with sotorasib in advanced solid tumors. N Engl J Med 2020;383:1207–17.
51. Awad MM, Liu S, Rybkin II, Arbour KC, Dilly J, Zhu VW, et al. Acquired resistance to $KRAS^{G12C}$ inhibition in cancer. N Engl J Med 2021;384:2382–93.
52. Bear AS, Blanchard T, Cesare J, Ford MJ, Richman LP, Xu C, et al. Biochemical and functional characterization of mutant KRAS epitopes validates this oncoprotein for immunological targeting. Nat Commun 2021;12:4365.
53. Padovan E, Bauer T, Tongio MM, Kalbacher H, Weltzien HU. Penicilloyl peptides are recognized as T cell antigenic determinants in penicillin allergy. Eur J Immunol 1997;27:1303–7.
54. Ostrov DA, Grant BJ, Pompeu YA, Sidney J, Harndahl M, Southwood S, et al. Drug hypersensitivity caused by alteration of the MHC-presented self-peptide repertoire. Proc Natl Acad Sci U S A 2012;109:9959–64.
55. Adams JJ, Narayanan S, Liu B, Birnbaum ME, Kruse A, Bowerman NA, et al. T cell receptor signaling is limited by docking geometry to peptide-major histocompatibility complex. Immunity 2011;35:681–93.
56. Visscher M, Arkin MR, Dansen TB. Covalent targeting of acquired cysteines in cancer. Curr Opin Chem Biol 2016;30:61–7.
57. Cross DAE, Ashton SE, Ghiorghiu S, Eberlein C, Nebhan CA, Spitzler PJ, et al. AZD9291, an irreversible EGFR TKI, overcomes t790m-mediated resistance to EGFR inhibitors in lung cancer. Cancer Discov 2014;4:1046–61.